Polarized X-ray absorption spectroscopy and XPS of TiS₃: S K- and Ti L-edge XANES and S and Ti 2p XPS

M.E. Fleet *, S.L. Harmer, X. Liu, H.W. Nesbitt

Department of Earth Sciences, University of Western Ontario London, Ont., Canada N6A 5B7

Abstract

Sulfur and Ti 2p XPS and polarized S K- and L$_{2,3}$- and Ti L$_{2,3}$-edge XANES spectra have been obtained from oriented ribbon-like crystals of TiS$_3$ grown by vapor transport. The S 2p XPS spectrum for (001) crystal faces has line widths of 0.53 eV and is completely accounted for by partially overlapped 2p$_{3/2}$/2p$_{1/2}$ doublets for sulfide (S^{2-}) and disulfide (S$_2^{2-}$) species, which are separate and independent entities in TiS$_3$. Evidence of unsaturated surface states is lacking, consistent with a surface monolayer for the (001) growth face of disulfide atoms oriented with their charge-neutral sides outward. The S K-edge XANES spectra show pronounced anisotropy in the (001) plane of TiS$_3$ crystals, associated with the photoelectron transition channel S 1s → 3p$_x$σ$_u^*$ with the electric vector (**E**) parallel the *a*-axis (and the S–S bond of the disulfide group), and transitions to unoccupied antibonding orbitals of S–Ti bonds with **E** parallel to the *b*-axis (the direction of the well-known quasi-one-dimensional character of TiS$_3$). The XPS and ultrasoft and soft X-ray region XANES spectra confirm the surface and near-surface structural integrity of TiS$_3$.
© 2005 Elsevier B.V. All rights reserved.

Keywords: X-ray photoelectron spectroscopy; X-ray absorption near edge spectroscopy; Sulfides; Layered structures; TiS$_3$

1. Introduction

Titanium trisulfide (TiS$_3$) is a low-dimensional, van der Waals' bonded, layered transition-metal sulfide [1,2]. It belongs to the class of alkali-metal-insertable chalcogenides used in CuO-based cathodes of non-aqueous alkali metal batteries [3]. Consequently, its synthesis [4,5], chemical spectroscopy [6–10], electronic structure [7,11], electrical and magnetic properties [12–15] and single-crystal anisotropy [8,9] have been well studied. The compound has a relatively low-temperature stability, undergoing peritectic decomposition at 632 °C, 8.95 atm.

Titanium trisulfide crystallizes with the monoclinic ZrSe$_3$-type crystal structure, in space group

---

* Corresponding author. Tel.: +1 519 661 3184; fax: +1 519 661 3198.

E-mail address: mfleet@uwo.ca (M.E. Fleet).

$P2_1/m$, with $a = 4.958$, $b = 3.4006$, $c = 8.778$ Å, and $\beta = 97.32°$ [1,2] (Fig. 1). Two of the three sulfur atoms per formula unit are present as a single-bonded disulfide ion (S_2^{2-}; S–S = 2.04 Å), and the third sulfur atom is formally sulfide (S^{2-}). The Ti
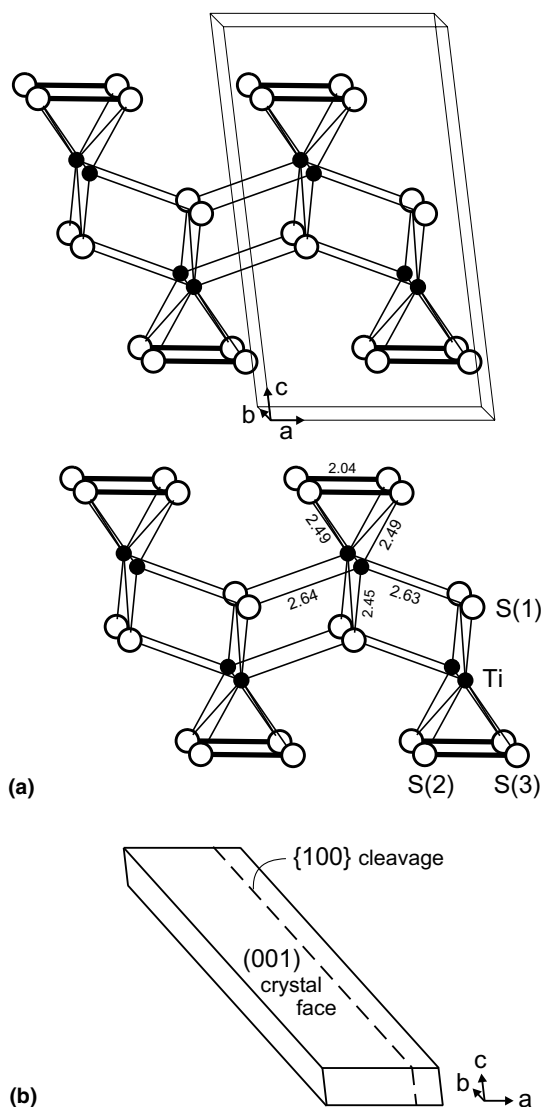

(a)

(b)

Fig. 1. (a) Structure of TiS$_3$ (type A) extending over about eight unit cells: solid circles are Ti; open circles are S, S(1) is sulfide (S^{2-}) and S(2) and S(3) are disulfide (S_2^{2-}); bond distances are in angstrom; note that S–S bonds of disulfide groups (heavy lines) are parallel to a-axis. (b) Sketch of ribbon-like crystal of TiS$_3$ in crystallographic orientation of part (a).

atom is in irregular eightfold coordination with sulfur atoms. Six shorter Ti–S distances (of 2.45–2.49 Å) form TiS$_6$ trigonal prisms which are linked via shared faces into an infinite chain parallel to the b-axis, making the structure quasi-one-dimensional. Neighboring chains are offset by $b/2$ and connected laterally via longer Ti–S bonds (of 2.63 and 2.64 Å) into sheets parallel to the crystal face (001). Individual (001) sheets are bounded above and below by a layer of disulfide groups, and held together in the resulting two-dimensional structure only by weak (van der Waals') forces. Importantly for the present study, the bond axis of the disulfide group is aligned parallel to the crystallographic a-axis.

Sulfur 2p X-ray photoelectron spectroscopy (XPS) measurements have been made on TiS$_3$ [7,10] and, earlier, on the isostructural compound ZrS$_3$ [11]. Jellinek et al. [11] deduced a molecular orbital scheme for the disulfide ligand in the ground state of these two trisulfide compounds, showing that the lowest unoccupied antibonding orbital ($3p_x\sigma_u^*$) is projected parallel to the S–S bond axis. The marked anisotropy of the TiS$_3$ structure has been investigated by polarized infrared [8], Raman [16], and micro-Raman [9] spectroscopy. All of these vibrational studies reported markedly different spectra for light polarized parallel and perpendicular to the direction of the chain of TiS$_6$ trigonal prisms (b-axis), and [8] inferred a rather weak interchain interaction from the very small frequency differences between the Raman active and infrared active Γ point phonons. X-ray absorption spectroscopy is also sensitive to anisotropy of crystal structure because the absorption edge features are dependent on both the initial and final electron states, thus permitting the anisotropy of conduction states to be probed. Layer-structure compounds, like the transition-metal chalcogenides, hexagonal nitrides, and V$_2$O$_5$, have been particularly well studied in this respect [17–21]. The last of these studies investigated the polarized X-ray absorption of the hexagonal CdI$_2$-structure chalcogenides TiS$_2$, TiSe$_2$ and TiTe$_2$, which have uniaxial physical (optical, electric, magnetic) properties and maximum anisotropy parallel to the c-axis. We presently investigate the polarized X-ray absorption of

TiS$_3$ at the S K- and L- and Ti L-edges. Whereas, the layered-structure MX$_2$ chalcogenides (M = Ti, Zr, Hf, V, Nb, Ta, Mo, and W; X = S, Se and Te) are isotropic perpendicular to the *c*-axis, TiS$_3$ is anisotropic both parallel and perpendicular to the layer normal (d_{001}), permitting a more direct correlation between polarized absorption and orientation of unoccupied antibonding orbitals. Also, we show that a high-resolution S 2p XPS spectrum for TiS$_3$ is in precise agreement with the assumed valence states of the sulfur atoms, and confirm the absence of reconstruction surface states on the (001) growth surface.

2. Experimental methods

2.1. Synthesis

Crystals of TiS$_3$ were synthesized by vapor transport in sealed evacuated silica glass tubes, of 7 mm internal diameter and about 170 mm in length. Charges were prepared from stoichiometric mixtures of high-purity Ti sponge and elemental sulfur, and reacted in a horizontal furnace at 400–600 °C for eight days, with the starting mixture positioned in the furnace hot spot. The vapor-transported products comprised millimeter-sized crystals of TiS$_3$ and TiS$_2$, as well as elemental sulfur. These phases were spatially separated at the cold end of the tubes, facilitating an essentially pure sampling of the TiS$_3$ crystals. The titanium sulfides were characterized by powder and single grain X-ray diffraction, using Rigaku DMAX II (Cu Kα X-radiation), Rigaku D/MAX-B system (Co Kα) and Bruker D8 Discover (Cu Kα) diffractometer and Gandolfi camera (Cr Kα) procedures. The type A structure for TiS$_3$ was confirmed using the X-ray diffraction criteria of Furuseth and Fjellvåg [2]. Crystals were elongated in the *b*-axis direction (Fig. 1b). The larger crystals were blade- or ribbon-like on (001) with a perfect 100 cleavage and up to $30 \times 0.3 \times 0.005$ mm^3 in size, but overall crystal thickness was highly variable, grading downwards to <1 μm for fibres and whiskers. Cadmium iodide-type TiS$_2$ was prepared from a stoichiometric mixture of Ti sponge and elemental sulfur contained in a sealed evacuated silica glass

tube and reacted in a box furnace at 500 °C overnight and 700 °C for 2 h. The product was then crushed, re-tubed and heated at 1200 °C for 1 h and 1000 °C for 60 h, and quenched in water.

2.2. XANES

Sulfur K- and L- and Ti L-edge XANES spectra were collected at the Canadian Synchrotron Radiation Facility (CSRF), Aladdin storage ring (University of Wisconsin at Madison, Wisconsin), using simultaneous measurements in fluorescence yield (FY) and total electron yield (TEY) modes, with the latter indicated by current yield measured at the sample holder. The storage ring was operated at 800 MeV, 60–180 mA. Sulfur K- and L-edge spectra were measured on a double crystal monochromator (DCM) beamline [22] and a Mark IV Grasshopper monochromator beamline [23], respectively. The DCM used an InSb (111) crystal and had an energy resolution of about 0.6 eV (FWHM) at 1840 eV; the Darwin width of the crystal corresponds to an energy resolution of 0.9 eV for the S K edge. The double Bragg reflection geometry results in a beam at the sample that is essentially 100% polarized for the S K edge [24]. The beam size at the sample was <1 × 3 mm^2. The grasshopper beamline used an 1800/mm holographic grating with an energy resolution of <0.1 eV in the S L-edge region. The beam height at the sample was ∼1 mm. The TEY recording mode probes the near surface (estimated at <100 Å depth for the S K edge and <50 Å depth for the S L edge), whereas the FY mode is more representative of the bulk material [25,26]. As recently noted [27], our S K-edge XANES spectra of labeled sulfur compounds compare very favorably with measurements on more recent generation beamlines fitted with a Si(111) monochromator [28]. This is because the core–hole lifetime broadening is significantly greater than the resolution of the Si(111) crystal. Also, the edge feature (or white line) of the XANES spectra is often considerably broadened by fine structure reflecting complexity in the final states. Kravtsova et al. [27] emphasized that no new features were evident in S K-edge XANES spectra of metal monosulfides recorded using a Si(111) monochromator.

Sample mounts were prepared using double-sided conducting carbon tape affixed to a clean stainless steel disk. All operations for the grasshopper and spherical grating monochromator (SGM) beamlines, including opening the silica glass tubes and preparation of the mounts, were conducted in a dry nitrogen-filled glove bag attached to the port of the spectrometer sample chambers [27,29]. For collection of polarized absorption spectra, a textured (oriented) mount was prepared by carefully laying larger blade-like crystals of TiS_3 in parallel alignment on the carbon tape. After collection of the S L-edge spectra, the textured mount was transferred to the DCM beamline with minimal exposure to air. A separate textured mount was prepared for the Ti L-edge measurements (below). The experimental design for XANES measurements on all three beamlines allowed the electric vector (**E**) of the synchrotron radiation to be oriented, at normal incidence [wave vector **k** normal to $(0\,0\,1)$], parallel to either the *a*-axis or the *b*-axis; i.e., corresponding to **E** perpendicular and parallel to the elongation of the textured crystals, respectively (Figs. 1 and 2). In addition, the $(0\,0\,1)$ plane of the crystals could be tilted through an angle θ up to 75° relative to **E**, with the tilt angle set visually to within ±3°. The useful range of θ for the DCM beamline was limited by interference from the frame of the sample holder to about 0–60°. Powder samples of TiS_3 and TiS_2 were prepared by lightly grinding a 1:1 mixture of sulfide crystals and powdered quartz in an agate mortar.

The DCM (S K-edge) measurement conditions included a photon energy range of 2455–2515 eV at a step size of 0.25 eV, with count times determined by counting statistics and two scans per sample, giving a total run time of approximately 29 min per sample. The grasshopper (S L edge) measurement conditions included a photon energy range of 150–190 eV at a step size of 0.07 eV and two scans per sample, with a total collection time of approximately 20 min per sample.

The SGM beamline used for collection of the Ti L-edge spectra was monochromatized by a 600 lines/mm grating over the photon region 240–670 eV, and yielded a photon resolution <0.25 eV at the Ti L-edge (~455 eV); the beamline
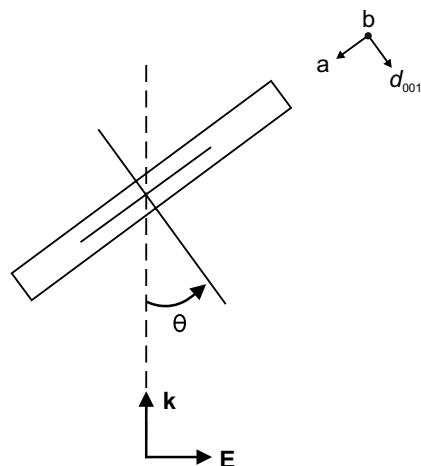

Fig. 2. Experimental design for collection of XANES spectra using textured sample mount: ribbon-like crystal of TiS_3 is viewed in projection down *b*-axis (cf., sketch in Fig. 1b); **k** is wave vector and **E** is electric vector of synchrotron radiation; θ is angle made by normal to $(0\,0\,1)$ and direct beam, and varied from 0° to about 75°. Two series of measurements were made: (1) crystal rotated about *b*-axis (as illustrated) and **E** parallel to the *a*-axis and S–S bond axis at $\theta = 0°$, and (2) crystal rotated about *a*-axis and **E** parallel to the *b*-axis and normal to S–S bond axis at $\theta = 0°$; note that, in the monoclinic crystal system, the interplanar spacing d_{001} is not parallel to *c*-axis, and its length is $[c \sin(\beta)]$.

delivered $>2 \times 10^{10}$ photons/s (when the stored electron beam is about 100 mA); the beam size at the sample was 1×1 mm^2, and the pressure at the sample was 10^{-8}–10^{-9} Torr. Measurement conditions included a photon energy range of 455–474 eV at a step size of 0.1 eV and one scan per sample, with a total collection time of approximately 8 min per sample.

Data reduction and analysis used the BAN and BGAUSS data analysis programmes [30] and FORTRAN77 codes. All XANES spectra were normalized against incident intensity (I_0), which was measured simultaneously, by current yield. Sulfur K-edge spectra were calibrated to the K-edge peak of native sulfur at 2472.0 eV [31], after removal of a linear pre-edge background. The Ti L-edge XANES spectra were calibrated relative to the Ti L-edge of rutile (TiO_2) at 458.23 eV [32]. Background subtraction was made with an empirical Shirley-like function [33] fitted to the pre-edge region. The background for these L-edge

spectra was unsystematic from sample to sample and complicated by the composite nature of the spectra. The adopted correction, albeit unconventional, appeared adequate for the present qualitative use of these spectra. Features in all of the present XANES spectra are accurate to ±0.1 eV.

2.3. XPS

X-ray photoelectron spectroscopy (XPS) measurements used a Kratos Axis Ultra instrument fitted with a monochromated Al Kα X-ray source (1487 eV) operated at 15 kV and 14 mA and a spot size of 300 μm. The detector was at normal incidence to the sample surface enabling analysis up to a depth of 50–100 Å. A textured sample of TiS$_3$ crystals was prepared in a glove box filled with dry Ar gas attached to the XPS spectrometer. The analytical chamber was maintained at 2×10^{-9} Torr. Survey spectra were collected using a pass energy of 160 eV and a step size of 0.7 eV, to check sample purity. High-resolution spectra were collected at 10 eV pass energy using a step size of 0.025 eV. All spectra were fitted by least-squares refinement, after subtraction of a Shirley background [33]. The spectrometer was standardized to the Au 4f peak at 84.0 eV and calibrated using the Cu 2p$_{3/2}$ peak at 936.6 eV.

3. Results and discussion

3.1. S 2p XPS spectrum

The S 2p XPS spectrum of TiS$_3$ obtained with the Kratos Axis Ultra (Fig. 3a) has been fitted with spin–orbit split doublet peaks for two sulfur species, interpreted as sulfide (S^{2-}) and disulfide (S$_2^{2-}$), using peak shapes of 50% Gaussian/50% Lorentzian (G:L ratio of 1:1). Corresponding pairs of S 2p$_{3/2}$ and S 2p$_{1/2}$ peaks were assigned the same peak width (FWHM) and separated by 1.19 eV [34,35], with the S 2p$_{1/2}$ peak assigned half the intensity of S 2p$_{3/2}$ according to theory. Thus, the binding energy, intensity and FWHM of the S 2p$_{1/2}$ peak were calculated entirely from the fitted parameters of the S 2p$_{3/2}$ peak. The G:L peak shape ratio of 1:1 was optimized by trial-and-

error. The refined values for S 2p$_{3/2}$ peak position and FWHM were 161.2 eV and 0.53 eV for the sulfide atom (S^{2-}) and 162.4 eV and 0.53 eV for the disulfide group (S$_2^{2-}$), and the disulfide/sulfide peak intensity ratio was 2.021.

The S 2p XPS spectrum of TiS$_3$ (Fig. 3a) is of exceptional resolution, and confirms the chemical state of the sulfur atoms inferred from earlier studies [7,10,11]. The XPS spectrum is seen to be composite, and comprised of three narrow, symmetric overlapped peaks representing S 2p$_{3/2}$ and S 2p$_{1/2}$ doublets for one sulfide (S^{2-}) atom and one disulfide (S$_2^{2-}$) group per formula unit, with the S 2p$_{1/2}$ limb of the S^{2-} doublet overlapping the S 2p$_{3/2}$ limb of the S$_2^{2-}$ doublet. The fitted peak widths for the sulfide (0.53 eV) and disulfide (0.53 eV) components are significantly smaller than in previous studies (e.g., 0.7–0.75 and 0.8 eV, respectively, in [10]), and result in minimal overlap of the three resolved spectral components. One of the most interesting aspects of the S 2p spectrum of TiS$_3$ is that the two sulfur doublets provide a complete fit to the spectrum. The fitted disulfide/sulfide peak intensity ratio of 2.021 is within error of the ideal value of 2, and confirms the stoichiometric integrity of the near-surface monolayers of the sample. It is evident that there is no measurable intervalent transfer between the two sulfur species: the sulfide and disulfide species are indeed separate and independent entities in titanium trisulfide.

The increased resolution of the new generation of conventional XPS instruments has produced spectra with much narrower peak widths than in previous studies. The present values of 0.53 eV are consistent with recent measurements of S 2p peak widths in transition-metal sulfides (0.41–0.55 eV [35–38]). As the inherent peak width measured in the gas phase is 0.12 eV, these experimental values for sulfides show that the resolution of the Kratos Axis Ultra is in the order of only 0.3 eV. Consequently, excess intensity attributable to surface chemical species formed as a result of fracture is now resolved routinely using conventional XPS instruments [35]. Although the Kratos system does not resolve surface states in the detail afforded by the highly surface sensitive techniques of synchrotron radiation XPS (SRXPS) [35–38] and synchrotron radiation photoemission [39],
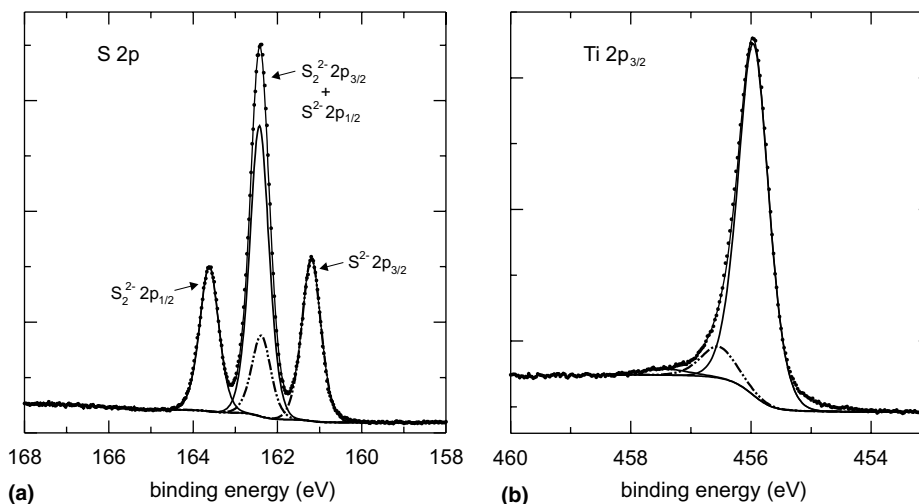
Fig. 3. XPS spectra for textured TiS$_3$ crystals: (a) S 2p, showing S 2p$_{3/2}$/S 2p$_{1/2}$ doublets for one sulfide (S^{2-}; dot-dot-dash peaks) and two disulfide (S$_2^{2-}$) atoms per formula unit; S 2p$_{3/2}$ peaks are at 161.2 eV for S^{2-} and 162.4 eV for S$_2^{2-}$; note that the S 2p$_{3/2}$ peak of S$_2^{2-}$ overlaps the S 2p$_{1/2}$ peak of S^{2-}. (b) Ti 2p$_{3/2}$: peak for pristine TiS$_3$ is at 455.9 eV; weak dot-dot-dash peak probably represents TiO.

there is a good correspondence between the binding energies of the excess intensity from conventional XPS and the surface states from SRXPS for fractured surfaces of pyrite (FeS$_2$), marcasite (FeS$_2$) and arsenopyrite (FeAsS) [35].

As their kinetic energy is about 1326 eV when using an Al Kα source, S 2p photoelectrons traverse approximately 15 monolayers before attenuation. Ignoring packing density [40,41], the bulk S 2p signal contributes 90–95% and the surface signal about 5–10% of the total sulfur intensity [40–42]. The majority of contemporary XPS studies of metal sulfides have revealed additional intensity resulting from surface atoms that have different chemical environments than the fully coordinated atoms in the bulk. In these covalently-bound compounds, surface atoms exist in a lower coordination than in the bulk due to removal of nearest-neighbor atoms as a result of fracture, cleavage or scraping, or at a terminal growth surface producing a high surface free energy. Stabilization of these surfaces may be achieved by lowering the surface free energy through redistribution of electrons on surface atoms or surface reconstruction [36,43,44].

No distinct surface signal, in the form of excess intensity on the high binding energy flanks of the

disulfide peaks [35], is observed in the Kratos S 2p XPS spectrum for TiS$_3$ (Fig. 3a). This conclusion is, of course, qualified by the limited resolution of the surface monolayer in conventional-source XPS analysis. However, based on the comparison of conventional and synchrotron radiation S 2p XPS spectra for pyrite-group sulfides in Fig. 2 of [35], we predict that additional (surface) features will not be prominently present in the equivalent SRXPS spectrum of TiS$_3$. The apparent absence of prominent surface states in the S 2p XPS spectrum of TiS$_3$ (Fig. 3a) is consistent with the surfaces analyzed, which are predominately (001) growth faces of the textured crystals (Fig. 1). By extension of this reasoning, the present XPS spectrum confirms that the surface monolayer of the (001) face of TiS$_3$ crystals is formed of disulfide atoms. These atoms are essentially charge neutral in respect to interactions in directions away from the TiS$_3$ layer units, forming only weak, van der Waals' bonds with disulfide atoms of adjacent layer units in the bulk structure. As no covalent or ionic bonds are broken at the (001) growth surface there is no need for surface stabilization. Breaking of van der Waals' bonds should not result in extensive reconstruction of the neighboring atoms as there is no sharing of

electrons. The atoms at the surface should have the same coordination as those in the bulk. Additionally, the absence of a high binding energy tail suggests that no ligand-to-metal transfer mechanism occurs in TiS_3.

3.2. Ti $2p_{3/2}$ XPS spectrum

The Ti $2p_{3/2}$ spectrum collected from the TiS_3 crystals (Fig. 3b) exhibits a strong peak centered at about 456 eV and a small high binding energy tail extending to about 458 eV. The G:L ratio was adjusted to provide the best fit to the main peak. The adopted value of 1:1 has a greater Lorentzian component than previous studies. As a result of more accurate electron analyzers, detectors and monochromated X-ray sources, the instrument response function is greatly reduced, thereby revealing the underlying inherent Lorentzian peak shape. A single symmetric peak was fitted along the leading edge of the Ti $2p_{3/2}$ spectrum at 456.0 eV with a FWHM of 0.6 eV, and is consistent with fully coordinated Ti^{4+} in the bulk. The binding energy of the Ti $2p_{3/2}$ peak is in agreement with that reported by [10] for TiS_3. Convergence of the refinement was obtained by fitting two peaks to the high binding energy tail with FWHM constrained to the value of the main peak.

Even with increase in the Lorentzian component of the G:L ratio, the fitted peak does not provide a good fit to the low binding energy side of the Ti $2p_{3/2}$ spectrum. Similar excess low binding energy intensity has been observed in the metal peaks of other sulfides, and remains incompletely understood [35,37]. Possible explanations include the presence of reduced Ti species at the surface and use of an incorrect G:L function in peak fitting. Reduced Ti may form at the surface as a result of defects or from X-radiation beam damage.

The two additional peaks fitted to the high binding energy tail of the Ti $2p_{3/2}$ spectrum have binding energies of 456.5 and 457.4 eV. As a sub-monolayer of O (1.95 at.%) was observed at the TiS_3 surface in the broad scan analysis and the Ti 2p tail contributes 2.3% to the total signal, these additional peaks (and high binding energy tail) are most likely due to minor TiO and Ti oxysulfide species, respectively [10].

3.3. XANES spectra

The polarized XANES spectra collected in the soft X-ray region from oriented crystals of TiS_3 using the total electron yield (TEY) are reported in Figs. 4–7. In all cases, the fluorescence yield spectra showed the same features as corresponding TEY spectra, but at inferior peak-to-background resolution. The S K-edge XANES (Figs. 4–6) are characterized by a prominent absorption edge feature (white line) a, which represents transition of the S 1s core electron to the lowest unoccupied antibonding states on the S atom restricted by the atomic selection rules $\Delta L = \pm 1$, $\Delta J = 0$ or ± 1, in the electric dipole approximation. For most S-bearing materials, peak a represents the photoelectron transition S $1s \rightarrow$ S $3p\sigma^*$. However, in transition-metal sulfides unoccupied antibonding states on the sulfur atoms may be hybridized with empty metal 3d states [27,29,45,46], to the extent that the white line of the S K edge may reflect aspects of the 3d electron configuration of the metal atom(s) [47,48]; e.g., the edge feature of CdI_2-type TiS_2 is split into two components a_1 and a_2 which apparently represent transition to S $3p\sigma^*$
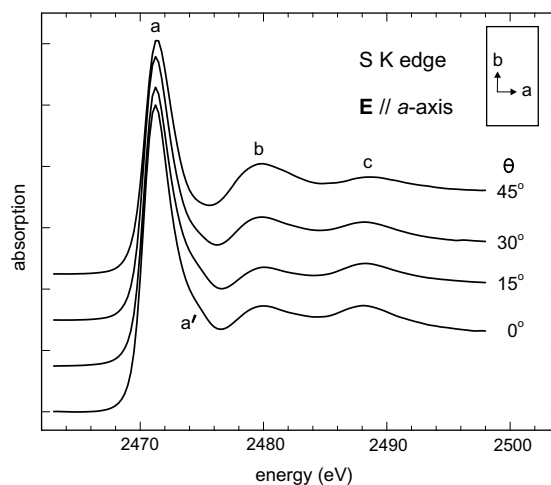

Fig. 4. S K-edge XANES spectra for textured crystals of TiS_3 oriented with the electric vector (**E**) parallel to *a*-axis at $\theta = 0°$, and rotated 15°, 30° and 45° about *b*-axis (cf., Fig. 2): inset shows orientation of individual ribbon-like crystal at $\theta = 0°$; spectra collected by TEY, and normalized to a common height for the edge jump.
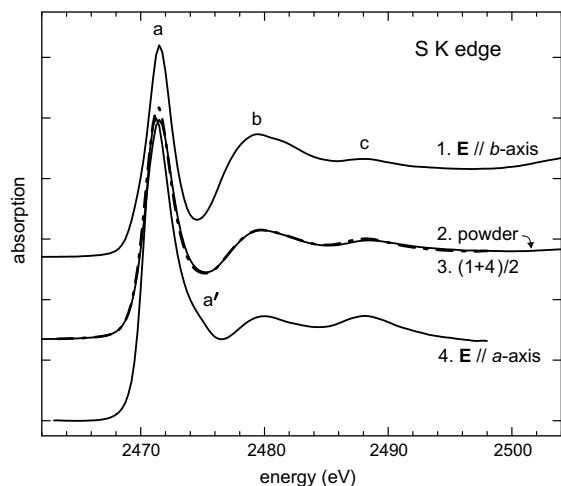
Fig. 5. S K-edge XANES spectra for TiS$_3$ crystals oriented with **E** parallel to *a*- and *b*-axes, **k** normal to (001), compared with spectra for the powdered sample and the average of the two crystal spectra (dot-dash line): spectra collected by TEY, and normalized to the edge jump.
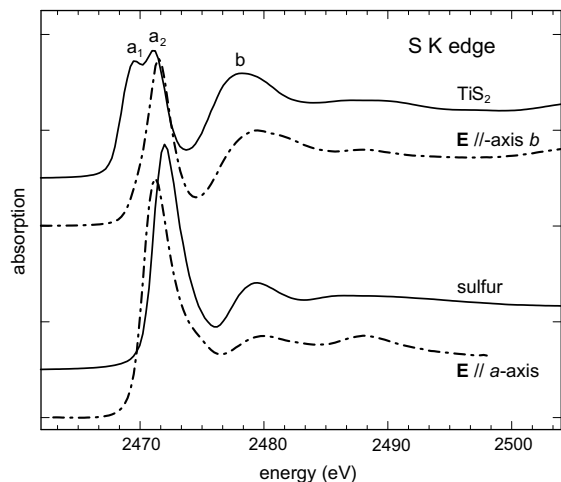

Fig. 7. Ti L$_{2,3}$-edge XANES spectra for TiS$_3$ crystals with **E** parallel to *a*- and *b*-axes [i.e., **E** parallel and normal to S–S bond axis, respectively, with **k** normal to (001)] and a powdered sample of TiS$_3$: features a, b, c, and d represent the Ti L$_3$ edge and f, g and h the Ti L$_2$ edge; spectra collected by TEY, and normalized to a common height for edge feature g.

Fig. 6. S K-edge XANES spectra for TiS$_3$ crystals oriented with **E** parallel to *a*- and *b*-axes [i.e., **E** parallel and normal to S–S bond axis, respectively, with **k** normal to (001); dot-dash lines], compared with XANES for powdered native sulfur and CdI$_2$-type TiS$_2$, respectively; spectra collected by TEY, and normalized to a common height for the edge jump.

antibonding states mixed with empty t$_{2g}$ and e$_g$ orbitals on Ti, respectively [47] (Fig. 6). The various post-edge features (b, c, etc.) of the S K-edge XANES are best attributed to multiple scattering
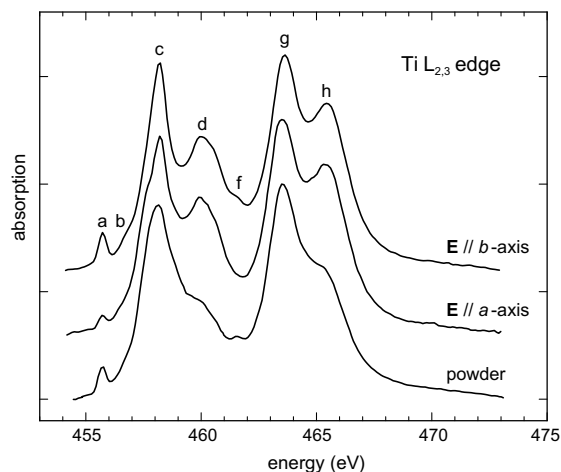
resonances. XANES spectra for the series of measurements starting with the electric vector (**E**) parallel to the *a*-axis and **k** normal to (001) (Fig. 4) have an additional feature a′ present as a shoulder on the high energy side of the edge feature. Although our spectrometer did resolve the splitting of the edge feature into components a$_1$ and a$_2$ for samples of CdI$_2$-type TiS$_2$ (Fig. 6) and the intercalated sulfide Ni$_x$TiS$_2$ ($x \rightarrow 0$), the S K edge of TiS$_3$ is clearly marked by a singlet feature.

Perhaps more significant is the apparent absence of evidence of composite structure in the XANES spectrum, because the K edge of TiS$_3$ represents absorption by two quite distinct sulfur species, S^{2-} and S$_2^{2-}$, and each of these sulfur species has an irregular bonding sphere. The two disulfide atoms [S(2) and S(3)] are both in pyramidal coordination with one S and two Ti atoms, in a S(STi$_2$) cluster (Fig. 1), whereas the single sulfide atom is in tetrahedral coordination with Ti and forms two short (2.45 Å) and two long (2.63, 2.64 Å) S–Ti bonds. The S K-edge feature of TiS$_3$ is located at about 2471.5 eV, compared with 2469.5–2470 eV for most transition-metal monosulfides, 2471 eV for disulfides of the pyrite-group, and 2472 eV for native sulfur [49,50]. On this basis,

the S K edge of TiS_3 might seem to be dominated by absorption associated with the two disulfide atoms. However, for a wide range of sulfur compounds, the white line of the S K edge shifts towards higher energy with increase in charge on the metal and decrease in the metallic/covalent character of the metal–S bond, being displaced as high as 2477 eV for the second edge peak of the ionically bound CaS [50]. Therefore, it is reasonable to assume that the K edge feature of the sulfide (S^{2-}) atom in TiS_3 is displaced upwards into near-coincidence with that of the two disulfide atoms.

The S L-edge XANES spectra of transition-metal sulfides are complicated by superposition of the L_3 and L_2 edges shifted by the spin–orbit splitting value of 1.1–1.2 eV, and the two dipole-allowed photoelectron transition channels ($2p \rightarrow 3s\sigma^*$) and ($2p \rightarrow 3d$) [27,29]. The spectra for TiS_3 were all similar to the S L-edge XANES of the isostructural compound ZrS_3 [51], and are not presently reported.

The Ti L-edge XANES spectra for the textured single crystals show excellent resolution of the L_3 and L_2 edges (Fig. 7), corresponding to the Ti $2p_{3/2}$ and Ti $2p_{1/2}$ excitations, respectively. The measured spin–orbit splitting is about 5.4 eV. Although the Ti 2p electron has dipole-allowed transitions to both s- and d-like final states, the 3d channel is much stronger than the 4s channel, due to the large wavefunction overlap. In consequence, the Ti 2p absorption is determined very largely by the transition probability for $3d^0 \rightarrow 2p^5 3d^1$. Both L_3 and L_2 edges are marked by two prominent features (c and d for L_3 and g and h for L_2) which are attributed to splitting of the 3d levels by the local crystal field of the Ti atom. The weak pre-edge features (a and b for L_3 and f for L_2) are probably attributable to multiplet core hole-3d electron interactions [52]. For octahedrally-coordinated Ti^{4+} in oxide lattices, c and g relate to transitions to empty $3d(t_{2g})$ orbital levels and d and h to transitions to empty $3d(e_g)$ levels [53–55]. The measured crystal field splittings for TiS_3 are 1.9 eV at the L_3 edge and 1.7 eV at the L_2 edge. The intensity relationships of the crystal field-split peaks in this sulfide are reversed compared with XANES spectra for Ti in four, five

and sixfold coordination in crystalline oxides and in silicate glasses [32], which consistently show relative absorption intensities of d > c and h > g [55]. Interestingly, measurement of the Ti L-edge XANES for CdI_2-type TiS_2, which has Ti in octahedral coordination, resulted in a spectrum unlike that of TiS_3 but similar to those of the Ti oxides, particularly Ba titanate which has Ti in fourfold coordination [32]. The sample mount for the present measurement on TiS_2 was prepared in air, so it is possible that the spectrum reflected contamination of the near surface of the sulfide with oxygen. In support of this suggestion, unpublished Ti L-edge study of binary Ti–S compositions with sample mounts prepared in air consistently yielded broadly similar TEY spectra, with d and h stronger than c and g, respectively, even though the corresponding FY spectra showed a progressive shift of all features to lower energy with decrease in the mean oxidation state of the Ti atoms. This observation may be evidence for the putative titanium oxysulfide thin-film phase [10]. Resolution of the second L_3, L_2-edge feature of TiS_3 (d and h, respectively; Fig. 7) was lost with light grinding of the sample in the glove bag, perhaps reflecting the fragility of the trichalcogenide crystal structure. However, all measurements on textured mounts of TiS_3 prepared in air resulted in a similar Ti $L_{2,3}$-edge XANES spectrum, suggesting that the loss in resolution of features d and h might also reflect minor incipient oxidation during grinding.

3.4. Polarization effects

Polarized absorption measurements were made with **E** first parallel to the *a*-axis of the TiS_3 crystals and **k** normal to (0 0 1) ($\theta = 0°$), and then inclined to the *a*-axis (and the plane of the structural layer unit) at angles (θ) of 15°, 30° and 45° by rotating the crystal about the *b*-axis (Fig. 2). Measurements were repeated with **E** first parallel to the *b*-axis and **k** normal to (0 0 1) ($\theta = 0°$), and then inclined to *b*-axis at angles of 15°, 30°, 45°, 60°, and 75°, by rotating about the *a*-axis. The experimental design, with the use of textured crystal mounts, allowed most of the crystal anisotropy to be investigated. When **E** is parallel to the *a*-axis ($\theta = 0°$), it is perpendicular to the TiS_6 trigonal pyramidal chain

but parallel to the S–S bond axis of the disulfide group (Figs. 1 and 2). Increase in θ tilts **E** away from the plane of the structural layer unit: **k** remains normal to the *b*-axis but is no longer normal to (001). Correspondingly, when **E** is parallel to the *b*-axis ($\theta = 0°$), it is parallel to the TiS_6 chain. Increase in θ tilts **E** away from the plane of the structural layer unit (and crystal elongation): **k** remains normal to the *a*-axis and the S–S bond axis but is no longer normal to (001).

Absorption anisotropy is pronounced for S K-edge measurements, particularly in the (001) plane of the crystals at $\theta = 0°$ (Figs. 5 and 6), but not for S and Ti L-edge measurements. For **E** parallel to the *a*-axis ($\theta = 0°$), and **k** normal to (001), the S K-edge feature a is more intense and is augmented by an additional feature a′, whereas the multiple scattering feature b is more prominent for **E** parallel to the *b*-axis, and **k** normal to (001). Also, the energy position of the edge feature a is characterized by shifts to 2471.3 eV for **E** parallel to the *a*-axis and 2471.5 eV for **E** parallel to the *b*-axis. The S K-edge XANES spectrum for the powdered sample is closely reproduced by the average of the two XANES spectra for **k** normal to (001) ($\theta = 0°$; Fig. 5). Increase in the tilt angle (θ) to 60° resulted in no significant change in the XANES spectra for the series of measurements starting with **E** parallel to the *b*-axis (and perpendicular to S–S bond axis). However, for the series of measurements starting with **E** parallel to the *a*-axis, significant change occurred at $\theta = 30°$ and 45°, with progressive diminution of the shoulder a′ and strengthening of the multiple scattering feature b (Fig. 4); the spectra collected at 60° and 75° were unusable due to interference from the sample holder. The S L- and Ti L-edge XANES spectra were similar for all orientations investigated (e.g., Fig. 7). However, the Ti L-edge spectrum for **E** parallel to the *a*-axis shows weaker pre-peak features (a and f) and evidence of complexity in the edge features c, d, g, and h. Increase in tilt angle resulted in some strengthening of the high-energy crystal field peaks (d and h) for both series of measurements, with a close approach to a common spectrum at the maximum tilt angle investigated (75°).

The minimal absorption anisotropy evident in the S and Ti L-edge XANES spectra of TiS_3 (e.g., Fig. 7) is readily accounted for, because transitions of core electrons to s final states are less likely to reveal crystal anisotropy than transitions to p and d states. Also, Ti^{4+} is in a fairly high (eightfold) irregular coordination with sulfur and less likely to show anisotropy for 3d orbital symmetry; see [56] for splitting of 3d states in the more strongly bonded TiS_6 trigonal prismatic cluster. Nevertheless, the first shell sulfur atoms are asymmetrically distributed, with four sulfide atoms on one side of the Ti atom and four disulfide atoms bridged by a strong σ bond on the other side, and the crystal field splitting of 5.4 eV revealed by the Ti L-edge XANES is moderate. In contrast, the S K-edge XANES spectra, which largely probe the s → p photoelectron transition channel, reveal strong absorption anisotropy in TiS_3. These observations are consistent with previous studies on layered structure compounds [17–20], where crystal orientation effects are less marked for L edges than K edges, and strongest for the K edge of the ligand atom(s): e.g., in an early study, strong anisotropy was evident at the Se K edge of the MoS_2-type diselenide WSe_2 but no anisotropy was discerned at the corresponding W L edge, nor at the Ta L edge of the CdI_2-type disulfide TaS_2 [17].

The maximum absorption anisotropy for TiS_3 occurs in the (001) plane of the layer unit, rather than normal to the layer unit as in the MX_2 chalcogenides [17,18,21], wurtzite-type nitrides [20], and V_2O_5 [19]. This difference in the orientation of the anisotropy is probably related to the presence of two strongly-bonded and mutually perpendicular features in the layer unit of the trisulfide: the TiS_6 chain (the quasi-one-dimensional structural unit) parallel to the *b*-axis and the disulfide group parallel to the *a*-axis (Fig. 1). Absorption with **E** parallel to the *b*-axis and the TiS_6 chain involves photoelectron transitions to antibonding states associated with resolved components of the four disulfide atom–Ti bonds and two short sulfide–Ti bonds. On the other hand, with **E** parallel to the *a*-axis, the absorption involves final states associated with the S–S bond [which gives rise to two interactions, S(2)–S(3) and S(3)–S(2)] and resolved components of the four disulfide atom–Ti bonds, with a minor contribution associated with the resolved components of the two long sulfide–Ti bonds.

We note that the disulfide group has the appropriate orientation and ground state electronic structure [7,11] to account for the anomalous absorption with **E** parallel to *a*-axis (Fig. 5). In particular, the abrupt decrease in strength of the shoulder a′ with increase in tilt angle θ beyond 15° (Fig. 4) is consistent with a dominant unidirectional bond. The only unoccupied S 3p antibonding orbital of the disulfide (S_2^{2-}) ion (S $3p_x\sigma_u^*$), is oriented along the S–S bond axis. The two S $3p_{y,z}$ antibonding orbitals are π-bonding in character and fully occupied within the valence band of the S_2^{2-} ion, leaving $3p_x\sigma_u^*$ as the dominant disulfide orbital of p character at the bottom of the conduction band of the crystal. Absorption due to the S $1s \rightarrow 3p_x\sigma_u^*$ transition is a maximum with **E** parallel to the *a*-axis of the TiS_3 crystals ($\theta \approx 0°$), because **E** is then parallel to the bond axis of the disulfide group. The absorption contributions from the S–S bond are expected to dominate the S K-edge XANES spectrum for this orientation.

In support of the present suggestion for dominance of the S–S bond for **E** parallel to the *a*-axis ($\theta = 0°$), note that the S K-edge XANES spectrum bears some similarity to that of native sulfur (and pyrite) but is quite unlike the S K-edge XANES of TiS_2, particularly in respect to the relative heights of features a and b, and the lack of evidence of p–d hybridization in the edge feature (Fig. 6). Conversely, when the crystals are oriented so that **E** is parallel to the *b*-axis (and normal to the S–S bonds), the S $1s \rightarrow 3p_x\sigma_u^*$ transition no longer operates. The final states for the s $\rightarrow$ p channel are now predominantly unoccupied S s,pσ* antibonding orbitals associated with S–Ti bonds. In consequence, the S K-edge spectrum for **E** parallel to the *b*-axis ($\theta = 0°$) bears some similarity to the S K-edge XANES of TiS_2 (Fig. 6).

The absence of crystal field splitting in the edge feature a shows that p–d hybridization, which is so important in defining final states for TiS_2 and many other transition-metal sulfides, is suppressed in S K-edge XANES spectra of TiS_3. This may be related to the unusual stereochemical feature of bridging S–S bonds in the first coordination sphere of Ti (Fig. 1a), which could have displaced the Ti 3d orbitals out of energy alignment with the empty S 3p antibonding orbitals. It is also noteworthy

that TiS_3 is diamagnetic [12], whereas CdI_2-type TiS_2 displays weak Curie–Weiss paramagnetism [57] and, hence, probably has a finite, albeit low, occupancy of Ti 3d states. The disulfide ion is well known to impose a low-spin 3d electron configuration and diamagnetic character on pyrite (FeS_2) [58]. Analogously to TiS_3, the S K-edge XANES spectrum of pyrite does not display crystal field splitting [49].

We recognize that the high energy shoulder (a′) to the edge feature of XANES spectra for the series of measurements starting with **E** parallel to the *a*-axis ($\theta = 0°$; Fig. 4) could reflect a degree of mixing of empty S $3p_x\sigma_u^*$ and Ti 3d orbitals, as was suggested analogously for a similar feature in the S K-edge XANES of $2H$-MoS_2 [18]. However, we have noted above that p–d hybridization is very likely suppressed in TiS_3. Also, the relatively high energy of a′ (2473.9 eV), and its abrupt diminution with increase in inclination of **E** to the direction of the S–S bond axis, is more consistent with a multiple scattering satellite to the edge feature.

The component of the S K-edge white line presently associated with directed S–S bonds in TiS_3 is somewhat analogous to the σ-shape resonance of chemisorbed gas molecules [59], although the latter tends to occur as a broad multiple scattering feature in the immediate post-edge region. Inner-shell electron energy-loss spectroscopy (ISEELS), which in the limit of small momentum transfer yields information equivalent to XANES spectroscopy, is generally used in preference to XANES for the study of σ-shape resonances [60]. Finally, study of the bulk structure of strongly-bonded compounds of the light elements using either XANES or another electron energy-loss technique (electron energy-loss near-edge structure, ELNES) routinely reveals absorption edge fine structure attributable to differential bonding characteristics [61,62].

4. Conclusions

XPS and ultrasoft and soft X-ray region XANES spectroscopy confirm the surface and near-surface structural integrity of ribbon-like crystals of TiS_3 grown by vapor transport. The S 2p XPS spectrum for (0 0 1) crystal faces

has exceptionally narrow line widths (0.53 eV) and is completely accounted for by two overlapped doublets, for S^{2-} (S $2p_{3/2}$ at 161.2 eV) and S_2^{2-} (S $2p_{3/2}$ at 162.4 eV). There is no evidence of unsaturated surface states in this conventional-source XPS spectrum, showing that the disulfide atoms, which interconnect the TiS_3 layer units in the bulk through van der Waals' bonds, form the (0 0 1) growth surface monolayer. The Ti $2p_{3/2}$ XPS spectrum is dominated by a singlet line at 455.9 eV, in agreement with the 4+ oxidation state assumed for the bulk, with additional weak intensity corresponding to minor/trace TiO and Ti oxysulfide species at the surface.

Polarized X-ray absorption measurements revealed pronounced anisotropy in the (0 0 1) plane of textured crystals at the S K edge but not at the S and Ti L edges. When the electric vector (**E**) of the synchrotron radiation is parallel to the *a*-axis (and to the direction of the covalent S–S bonds), and the wave vector is normal to (0 0 1), the S K-edge XANES spectrum is dominated by the photoelectron transition channel S $1s \rightarrow 3p_x\sigma_u^*$. The S $3p_x\sigma_u^*$ antibonding orbital is oriented along the S–S bond axis and is the only unoccupied S 3p antibonding orbital of the disulfide ion. The XANES spectrum for this orientation is dominated by the edge feature and is generally similar to that of native sulfur. A markedly different S K-edge spectrum, with a weaker edge feature, results for **E** parallel to the *b*-axis, the direction of the well-known quasi-one-dimensional character of TiS_3. The final states are now unoccupied antibonding orbitals associated exclusively with resolved components of S–Ti bonds. XANES spectra measured simultaneously by total electron and fluorescence yield were essentially identical for all three absorption edges investigated, demonstrating that the near-surface structure is an adequate description of the bulk structure.

Acknowledgements

References

[1] S. Furuseth, L. Brattås, A. Kjekshus, Acta Chemica Scandinavica A 29 (1975) 623.
[2] S. Furuseth, H. Fjellvåg, Acta Chemica Scandinavica 45 (1991) 694.
[3] G.L. Holleck, J.R. Driscoll, Electrochimica Acta 22 (1977) 647.
[4] K. Oshima, M. Yokoyama, H. Hinode, M. Wakihara, M. Taniguchi, Journal of Solid State Chemistry 65 (1986) 392.
[5] H.S.W. Chang, D.M. Schleich, Journal of Solid State Chemistry 100 (1992) 62.
[6] K. Endo, H. Ihara, K. Watanabe, S. Gonda, Journal of Solid State Chemistry 39 (1981) 215.
[7] K. Endo, H. Ihara, K. Watanabe, S. Gonda, Journal of Solid State Chemistry 44 (1982) 268.
[8] S. Jandl, J. Deslandes, M. Banville, Infrared Physics 22 (1982) 327.
[9] P. Gard, F. Cruege, C. Sourisseau, O. Gorochov, Journal of Raman Spectroscopy 17 (1986) 283.
[10] D. Gonbeau, C. Guimon, G. Pfister-Guillouzo, A. Levasseur, G. Meunier, R. Dormoy, Surface Science 254 (1991) 81.
[11] F. Jellinek, R.A. Pollak, M.W. Shafer, Materials Research Bulletin 9 (1974) 845.
[12] H. Haakon, A. Kjekshus, E. Roest, A. Steffensen, Acta Chemica Scandinavia 17 (1963) 1283.
[13] S. Kikkawa, M. Koizumi, S. Yamanaka, Y. Onuki, S. Tanuma, Physica Status Solidi A 61 (1980) K55.
[14] P.L. Hsieh, C.M. Jackson, G. Gruener, Solid State Communications 46 (1983) 505.
[15] E. Finkman, B. Fisher, Solid State Communications 50 (1984) 25.
[16] D.W. Galliardt, W.R. Nieveen, R.D. Kirby, Solid State Communications 34 (1980) 37.
[17] S.M. Heald, E.A. Stern, Physical Review B 16 (1977) 5549.
[18] D. Li, G.M. Bancroft, M. Kasrai, M.E. Fleet, X.H. Feng, K.H. Tan, Physics and Chemistry of Minerals 22 (1995) 123.
[19] E. Goering, O. Müller, M. Klemm, M.L. denBoer, S. Horn, Philosophical Magazine B 75 (1997) 229.
[20] K. Lawniczak-Jablonska, T. Suski, Z. Liliental-Weber, E.M. Gullikson, J.H. Underwood, R.C.C. Perera, T.J. Drummond, Applied Physics Letters 70 (1997) 2711.
[21] S. Bocharov, G. Dräger, D. Heumann, A. Šimůnek, O. Šipr, Physical Review B 58 (1998) 7668.

[22] B.X. Yang, F.H. Middleton, B.G. Olsson, G.M. Bancroft, J.M. Chen, T.K. Sham, K. Tan, D.J. Wallace, Nuclear Instruments and Methods in Physics Research A 316 (1992) 422.

[23] K.H. Tan, G.M. Bancroft, L.L. Coatsworth, B.W. Yates, Canadian Journal of Physics 60 (1982) 131.

[24] Z. Hussain, E. Umbach, D.A. Shirley, J. Stöhr, J. Feldhaus, Nuclear Instruments and Methods 195 (1982) 115.

[25] J. Kawai, H. Adachi, S. Hayakawa, S.Y. Zhen, K. Kobayashi, Y. Gohshi, K. Maeda, Y. Kitajima, Spectrochimica Acta 49B (1994) 739.

[26] M. Kasrai, W.N. Lennard, R.W. Brunner, G.M. Bancroft, J.A. Bardwell, K.H. Tan, Applied Surface Science 99 (1996) 303.

[27] A.N. Kravtsova, I.E. Stekhin, A.V. Soldatov, X. Liu, M.E. Fleet, Physical Review B 69 (2004), 134109/1.

[28] M. Bonnin-Mosbah, N. Métrich, J. Susini, M. Salomé, D. Massare, B. Menez, Spectrochim. Acta B 57 (2002) 711.

[29] S.P. Farrell, M.E. Fleet, Physics and Chemistry of Minerals 28 (2001) 17.

[30] T. Tyliszcak, BAN Data Analysis Program, McMaster University, 1992.

[31] J.C. Fuggle, J.E. Inglesfield, Unoccupied electronic states: fundamentals for XANES, EELS, IPS and BISTopics in Applied Physics, vol. 69, Springer-Verlag, 1992.

[32] G.S. Henderson, X. Liu, M.E. Fleet, Physics and Chemistry of Minerals 29 (2002) 32.

[33] D.A. Shirley, Physical Review B 5 (1972) 4709.

[34] H.W. Nesbitt, M. Scaini, H. Höchst, G.M. Bancroft, A.G. Schaufuss, R. Szargan, American Mineralogist 85 (2000) 850.

[35] S.L. Harmer, H.W. Nesbitt, Surface Science 564 (2004) 38.

[36] S.L. Harmer, A.R. Pratt, H.W. Nesbitt, M.E. Fleet, American Mineralogist 89 (2004) 1026.

[37] S.L. Harmer, A.R. Pratt, H.W. Nesbitt, M.E. Fleet, Canadian Mineralogist, in press.

[38] S.L. Harmer, M. Tang, W. Skinner, H.W. Nesbitt, G.M. Bancroft, in preparation.

[39] J.A. Rodriguez, J. Hrbek, Z. Chang, J. Dvorak, T. Jirsak, A. Maiti, Physical Review B 65 (2002) 235414.

[40] M.P. Seah, W.A. Dench, Surface Interface Analysis 1 (1979) 2.

[41] D. Briggs, M.P. SeahPractical Surface Analysis, vol. 1, John Wiley & Sons, 1990.

[42] S. Tanuma, C.J. Powell, D.R. Penn, Surface and Interface Analysis 17 (1991) 911.

[43] W. Mönch, Semiconductor surfaces and interfaces, Ch. 13Springer Series in Surface Sciences, Springer-Verlag, 1995.

[44] A.S. Gibson, J.P. Lafemina, Structure of mineral surfaces. Physics and chemistry of mineral surfaces, in: P.V. Brady (Ed.), CRC Series in Chemistry and Physics of Surfaces and Interfaces, CRC Press, 1996.

[45] J.A. Tossell, Journal of Chemical Physics 66 (1977) 5712.

[46] A.V. Soldatov, A.N. Kravtsova, M.E. Fleet, S.L. Harmer, Journal of Physics: Condensed Matter 16 (2004) 7545.

[47] Z.Y. Wu, G. Ouvrard, C.R. Natoli, Journal de Physique IV France 7 (1997) C2-199.

[48] S.P. Farrell, M.E. Fleet, I.E. Stekhin, A. Kravtsova, A.V. Soldatov, X. Liu, American Mineralogist 87 (2002) 1321.

[49] D. Li, G.M. Bancroft, M. Kasrai, M.E. Fleet, X.H. Feng, K.H. Tan, Canadian Mineralogist 33 (1995) 949.

[50] M.E. Fleet, X. Liu, S.L. Harmer, P.L. King, Canadian Mineralogist, in press.

[51] J.G. Chen, Surface Science Reports 30 (1997) 1.

[52] J.P. Crocombette, F. Jollet, Journal of Physics: Condensed Matter 8 (1996) 5253.

[53] F.M.F. de Groot, J.C. Fuggle, B.T. Thole, G.A. Sawatzky, Physical Review B 41 (1990) 928.

[54] F.M.F. de Groot, J.C. Fuggle, B.T. Thole, G.A. Sawatzky, Physical Review B 42 (1990) 5459.

[55] G. van der Laan, I.W. Kirkman, Journal of Physics: Condensed Matter 4 (1992) 4189.

[56] R. Huisman, R. de Jonge, C. Haas, F. Jellinek, Journal of Solid State Chemistry 3 (1971) 56.

[57] L.E. Conroy, K.C. Park, Inorganic Chemistry 7 (1968) 459.

[58] J.A. Tossell, D.J. Vaughan, Theoretical Geochemistry: Applications of Quantum Mechanics in the Ear, Oxford University Press, 1992.

[59] J. Stöhr, J.L. Gland, W. Eberhardt, D. Outka, R.J. Madix, F. Sette, R.J. Koestner, U. Doebler, Physical Review Letters 51 (1983) 2414.

[60] F. Sette, J. Stöhr, A.P. Hitchcock, Chemical Physics Letters 110 (1984) 517.

[61] L.A.J. Garvie, P.R. Buseck, Mineralogical Society of America Reviews in Mineralogy 33 (1996) 821.

[62] M.E. Fleet, X. Liu, Physics and Chemistry of Minerals 28 (2001) 421.